



## Global scale models of the mantle flow field predicted by synthetic tomography models

A.L. Bull<sup>a,\*</sup>, A.K. McNamara<sup>a</sup>, T.W. Becker<sup>b</sup>, J. Ritsema<sup>c</sup>

<sup>a</sup> School of Earth and Space Exploration, Arizona State University, PO Box 871404, Tempe, AZ 85287-1404, USA

<sup>b</sup> Department of Earth Sciences, University of Southern California, 3651 Trousdale Pkwy, MC0740, Los Angeles, CA 90089-0740, USA

<sup>c</sup> 2534 C. C. Little Building, 1100 North University Ave, University of Michigan, Ann Arbor, MI 48109-1005, USA

### ARTICLE INFO

#### Article history:

Received 20 May 2009

Received in revised form 31 January 2010

Accepted 4 March 2010

Edited by: M. Jellink.

#### Keywords:

Global flow

Mantle convection

Resolution matrix

Seismic tomography

Isochemical

### ABSTRACT

Using a multi-disciplinary technique incorporating the heterogeneous resolution of seismic tomography, geodynamical models of mantle convection, and relationships derived from mineral physics, we investigate the method of using seismic observations to derive global-scale 3D models of the mantle flow field. We investigate the influence that both the resolution of the seismic model and the relationship used to interpret wavespeed anomalies in terms of density perturbations have on the calculated flow field. We create a synthetic seismic tomography model from a 3D spherical whole mantle geodynamic convection model and compare present-day global mantle flow fields from the original convection model and from a geodynamical model which uses the buoyancy field of the synthetic tomography model as an initial condition. We find that, to first order, the global velocity field predicted by the synthetic seismic model correlates well with the flow field from the original convection model throughout most of the mantle. However, in regions where the resolving power of the seismic model is low, agreement between the models is reduced. We also note that the flow field from the synthetic seismic model is relatively independent of the density–velocity scaling ratio used.

© 2010 Elsevier B.V. All rights reserved.

### 1. Introduction

Understanding the global-scale velocity field associated with convection in Earth's mantle has been a long-standing pursuit in the geophysical community. Such an understanding is essential to constrain plate driving forces, geoid variations, lithospheric stresses and the thermal and compositional structure of the mantle. If plate motions are prescribed at the surface, return flow and mantle tractions can be computed (Hager and O'Connell, 1981). Constraints on the buoyancy-driven component of flow outside subduction zones arrived with the advent of global seismic tomography (e.g., Dziewonski et al., 1977; Dziewonski, 1984; Woodhouse and Dziewonski, 1984) as seismic velocity anomalies were interpreted in terms of density perturbations (e.g., Hager et al., 1985; Hager and Clayton, 1989; Ricard and Vigny, 1989). Subsequently, several models of the large-scale velocity fields of the mantle have been proposed (e.g., Richards and Hager, 1984; Ricard et al., 1984, 1989; Forte and Peltier, 1987, 1991; Hager and Clayton, 1989; Hager and Richards, 1989; King and Masters, 1992; Forte et al., 1994; King, 1995; Lithgow-Bertelloni and Richards, 1998; Becker and O'Connell, 2001; Forte and Mitrovica, 2001) and have been

widely used to investigate upper mantle anisotropy (e.g., Becker et al., 2003; Gabor et al., 2003; Conrad et al., 2007); geoid undulations (e.g., Cadec and Fleitout, 1999; King and Masters, 1992); surface uplift (e.g., Gurnis et al., 2000); tectonic plate velocities (e.g., Becker and O'Connell, 2001; Conrad and Lithgow-Bertelloni, 2002; Becker, 2006); lithospheric stress field (e.g., Steinberger et al., 2001; Lithgow-Bertelloni and Guynn, 2004) and upper mantle thermal structure (e.g., Cammarano et al., 2003). Comparisons of computed parameters, such as heat flux, plate motions, geoid and lithospheric stresses with the observations help assess the success of the models (e.g., Steinberger and Calderwood, 2006).

The global-scale mantle flow field is typically calculated from the Stokes and continuity equations for a given density distribution and mechanical boundary condition. Currently, one method of deriving such a density structure relies on converting a seismic tomography model into a density field (i.e., buoyancy structure) using relationships from mineral physics. Although widely used, there are several caveats to this method. Firstly, the resolution of seismic tomography models is inherently spatially heterogeneous due to an uneven and incomplete seismic sampling of the mantle (Fig. 1) (e.g., Mégnin et al., 1997). Ritsema et al. (2007) showed that the inhomogeneous data coverage and the damping applied in tomographic inversions result in suppressed short wavelength structures, removal of strong velocity gradients and artificial stretching and tilting of shear-wave velocity anomalies

\* Corresponding author.

E-mail address: [abigail.bull@asu.edu](mailto:abigail.bull@asu.edu) (A.L. Bull).

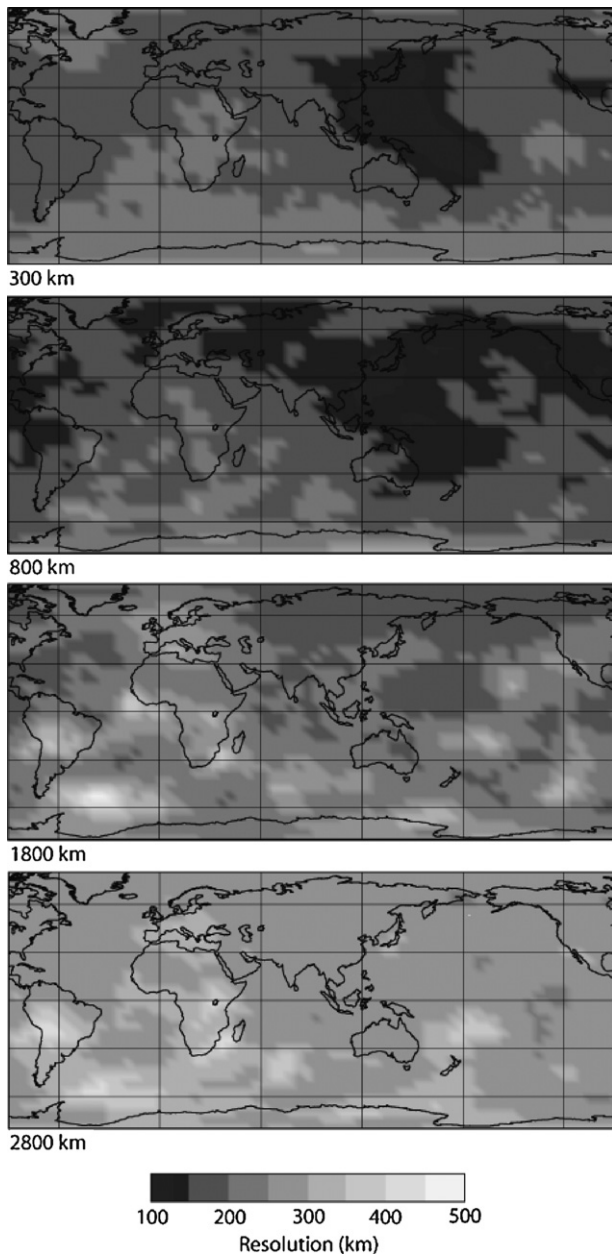


**Fig. 1.** Map of the resolving power of the tomographic model S20RTS (Ritsema et al., 1999, 2004) shown at 300 km, 800 km, 1800 km and 2800 km depth in the mantle. Darker colors represent areas of better resolution. Note the decrease in resolving power with depth in the lower mantle.

throughout the mantle. As such, if the tomographic model used to derive a density field distorts thermal and chemical heterogeneity in the mantle, the result will be a blurred image of mantle structure (e.g., Schubert et al., 2004; Ritsema et al., 2007; Bull et al., 2009; Schuberth et al., 2009) which could potentially lead to significant misinterpretations and uncertainties when this density field is used to calculate the instantaneous flow field. Secondly, the interpretation of the seismic wavespeeds in terms of density perturbations depends on relations derived from mineral physics (e.g., Karato and Karki, 2001; Stixrude and Lithgow-Bertelloni, 2005). Estimates of the relationship between observed seismic wavespeed anomalies and density defined as:

$$R_{\rho/V_s} = \frac{\delta \log \rho}{\delta \log V_s} \quad (1)$$

vary from  $-0.2$  to  $0.4$  for most materials, however there is no clear consensus on how to apply a pressure-dependence to the relationship over the depth of the mantle (e.g., Chopelas, 1992; Karato, 1993; Karato and Karki, 2001; Cammarano et al., 2003). Accordingly, most studies use constant values of the velocity–density relationship as a function of depth. One key issue in interpreting the tomographic model is whether the observed seismic anomalies have a thermal or chemical origin and how to translate that to density. As a result, several different formulations have been used. These include ignoring velocity or density variations in the uppermost 200–300 km of the mantle where the velocity structure is thought to be dominated by chemical heterogeneity (e.g., Jordan, 1978; Thoraval and Richards, 1997; Lithgow-Bertelloni and Silver, 1998), using a constant value for  $R$  throughout the upper mantle and allowing  $R$  to vary smoothly in the lower mantle (e.g., Forte et al., 1995; Cammarano et al., 2003), using a constant value throughout the entire mantle below 200 km (e.g., Steinberger et al., 2001), imposing near-zero or negative values in the lowermost mantle (e.g., Gurnis et al., 2000; Karato and Karki, 2001; Matas and Bukowinski, 2007), and determining the relationship through probabilistic tomography (e.g., Resovsky and Trampert, 2003). As such, global-scale mantle flow fields derived using this method may be subject to scaling errors that arise from imperfect or insufficient mineral physics data. Although it is possible to use self-consistent thermodynamic calculations (e.g., Stixrude and Lithgow-Bertelloni, 2005) to derive temperature-, pressure- and compositional-dependent seismic wavespeeds throughout the depth of the mantle, such an approach relies upon knowledge of the compositional structure of the mantle. We have used this approach in previous work (Bull et al., 2009); however in this work, we focus on investigating more classical approaches to density–wavespeed conversions.

One way to investigate the method of using seismic observations to derive global-scale 3D models of the mantle flow field is to run joint seismological and geodynamic inversions (e.g., Simmons et al., 2007). Here, we focus on a different approach and use a multi-disciplinary technique developed in previous work (Ritsema et al., 2007; Bull et al., 2009) to investigate the use of seismic tomography observations to mantle flow field models. We investigate how (1) the resolution of the seismic model and (2) the relationship used to interpret wavespeed anomalies in terms of density perturbations affect the calculated flow field. We create a synthetic tomography model from a 3D spherical whole mantle geodynamic convection model using the resolution matrix of the seismic tomography model, S20RTS (Ritsema et al., 1999, 2004), as an effective “seismic filter” to capture the variable resolution inherent to seismic tomography. We compare flow patterns of the global mantle flow fields from both the original convection model which serves as the control case and from a similar convection model that differs in that it uses the buoyancy field derived from the synthetic tomography model of the control case as an initial condition.

We find that, to first order, the global velocity field predicted by the synthetic tomography model correlates well with the flow field from the original convection model throughout most of the mantle, however in regions where the resolving power of the seismic model is low, agreement between the models is reduced. We also note that the flow field from the synthetic tomography model is relatively independent of the density–velocity scaling ratio used for the four typical profiles investigated in this work.

## 2. Method

### 2.1. Global-scale velocity field from the geodynamics model

Following the general approach of Davies and Bunge (2001), we calculate the global-scale mantle flow field using the 3D spherical

finite-element convection code CitcomS (Zhong et al., 2000) to solve an instantaneous Stokes flow calculation for a whole-mantle convection model. For this global circulation model (GCM), we impose a free-slip boundary condition at the surface. To create an initial condition for the GCM we first use CitcomS to solve a time-dependent convection calculation over the past 119 million years using surface plate motions as kinematic boundary conditions to guide the location of subduction (e.g., Bunge et al., 1998; Lithgow-Bertelloni and Richards, 1998; McNamara and Zhong, 2005). This initial calculation provides a model representation of slab and plume scale flow.

The non-dimensional equation for the conservation of mass in incompressible flow is:

$$\nabla \cdot \mathbf{u} = 0 \quad (2)$$

where  $\mathbf{u}$  is the velocity vector.

The non-dimensional momentum equation is

$$-\nabla P + \nabla \cdot (\eta \hat{\epsilon}) = (RaT)\hat{\mathbf{r}} \quad (3)$$

where  $\hat{\mathbf{r}}$  is the radial unit vector,  $P$  is the dynamic pressure,  $\eta$  is the viscosity,  $\hat{\epsilon}$  is the strain rate tensor,  $T$  is the temperature and  $Ra$  is the thermal Rayleigh number defined as

$$Ra = \frac{\alpha \rho g \Delta T h^3}{\eta \kappa} \quad (4)$$

where  $\alpha$  is the thermal expansivity,  $\rho$  is the density,  $g$  is the acceleration due to gravity,  $\Delta T$  is the temperature drop across the mantle,  $h$  is the mantle thickness and  $\kappa$  is the thermal diffusivity. We employ a Rayleigh number of  $2.8 \times 10^8$ . However, the overall effective Rayleigh number is much smaller given the depth dependence of viscosity, as shown below.

The non-dimensional heat equation is

$$\frac{\partial T}{\partial t} + (\mathbf{u} \cdot \nabla)T = \nabla^2 T + H \quad (5)$$

where  $t$  is time and  $H$  is the non-dimensional internal heating rate.

We employ a temperature- and depth-dependent rheology of the non-dimensional form:

$$\eta(T, \bar{z}) = \eta_r(z) \exp[A(0.5 - T)] \quad (6)$$

where  $\eta$  and  $z$  are the non-dimensional viscosity and dimensional depth respectively and  $\eta_r(z) = 1$  for  $z < 665$  km and  $\eta_r(z) = 0.1225z - 51.2$  for  $665 \text{ km} \leq z \leq 2850$  km. This formulation leads to a weak upper mantle, a  $30\times$  viscosity step increase at the boundary between the upper and lower mantle, and a  $10\times$  linear increase with depth to the base of the mantle. The non-dimensional activation coefficient,  $A$ , is chosen to be 9.2103, which leads to a temperature-induced viscosity contrast of  $10^4$ . The models are heated from below and internally (ratio of internal to bottom heating is approximately 1:1) with a dimensional heat production of  $0.01375 \text{ W m}^{-2}$ .

The temperature field resulting from the initial time-dependent numerical calculation is used as the initial condition for the calculation of instantaneous Stokes flow. The resulting global-scale flow field will be referred to as the ‘‘GCM flow field’’.

## 2.2. Global-scale velocity flow field from the synthetic tomography model

We convert the geodynamical temperature field to a temperature-dependent synthetic shear-wave velocity field using a velocity–density scaling relationship derived from mineral physics (e.g., Karato and Karki, 2001; Stixrude and Lithgow-Bertelloni,

2005):

$$R_{\rho/V_s} = \frac{\delta \log \rho}{\delta \log V_s} \quad (7)$$

where  $V_s$  is the shear-wave velocity and  $\rho$  is the density. Using:

$$\frac{\delta \rho}{\rho} = -(T - T_{ave})\alpha \quad (8)$$

Eq. (7) becomes:

$$T = T_{ave} - \frac{1}{\alpha} R \left( \frac{\delta V_s}{V_s} \right) \quad (9)$$

where  $T$  is the temperature,  $T_{ave}$  is the average temperature and  $\alpha$  is the coefficient of thermal expansion (taken to be  $2 \times 10^{-5} \text{ K}^{-1}$ ). Values for  $T_{ave}$  are taken from the original geodynamic calculation. For this work we employ four different depth-dependent relationships,  $R$  (Fig. 2) following previous studies (e.g., Gurnis et al., 2000; Karato and Karki, 2001; Steinberger and Calderwood, 2006; Steinberger and Holme, 2008). All cases assume a value of  $R=0$  in the uppermost 200 km of the mantle to account for effects of the tectosphere, as it is suggested that compositional differences are likely to cancel out the observed high-velocity anomalies beneath cratons (e.g., Jordan, 1978; Forte et al., 1995).

We first project the calculated seismic velocity field into the same spatial parameterization as the tomographic model S2ORTS (Ritsema et al., 1999, 2004) and then convolve it with the resolution operator of S2ORTS as described briefly below and in detail in Ritsema et al. (2007) to create a synthetic seismic model. This procedure will have two effects on the original temperature field. Firstly, any buoyancy structure above spherical harmonic  $20^\circ$  will be removed as S2ORTS is a  $20^\circ$  model, meaning that there is no power at shorter wavelengths. Secondly, the data will be smoothed due to the limited resolution of heterogeneity at the highest degrees.

A tomographic model is most commonly calculated from an observed seismic wavespeed in a linear fashion using

$$\mathbf{Gm} = \mathbf{d} \quad (10)$$

where  $\mathbf{d}$  is a vector of seismic data observations,  $\mathbf{m}$  is a vector of Earth model parameters and  $\mathbf{G}$  is a matrix which describes the geometry and physics of the problem and which relates the number of observations to the number of model unknowns. To construct the tomographic model, a value of  $\mathbf{m}$  must be calculated which satisfies Eq. (10) at least approximately, and thus the inverse of  $\mathbf{G}$  must be found.  $\mathbf{G}$  is not square (there are more constraints than model parameters) and it is ill-posed (certain areas of the mantle are sampled poorly) and therefore it cannot be directly inverted. It is thus usual to find  $\mathbf{m}$  by damped least-squares inversion:

$$\mathbf{m} = [\mathbf{G}^T \mathbf{G}]^{-1} \mathbf{G}^T \mathbf{d} \quad (11)$$

To analyze the degree of detail in the true model,  $\mathbf{m}_{true}$  that has been resolved, Eq. (11) can then be expressed as:

$$\mathbf{m}_{estimated} = [\mathbf{G}^T \mathbf{G}]^{-1} \mathbf{G}^T \mathbf{Gm}_{true} \quad (12)$$

where the resolution operator,  $\mathbb{R}$  is given by:

$$\mathbb{R} = [\mathbf{G}^T \mathbf{G}]^{-1} \mathbf{G}^T \mathbf{G} \quad (13)$$

(e.g., Soldati and Boschi, 2005)  $\mathbb{R}$  indicates how much the true model is smeared into the various parameters of the inversion model and leads to:

$$\mathbf{m}_{observed} = \mathbb{R} \mathbf{m}_{true} \quad (14)$$

For perfect model resolution,  $\mathbb{R}$  is 1 so the true model would be fully mapped into the inversion model. However, almost always  $\mathbf{m}_{observed}$ , represents a blurred image.

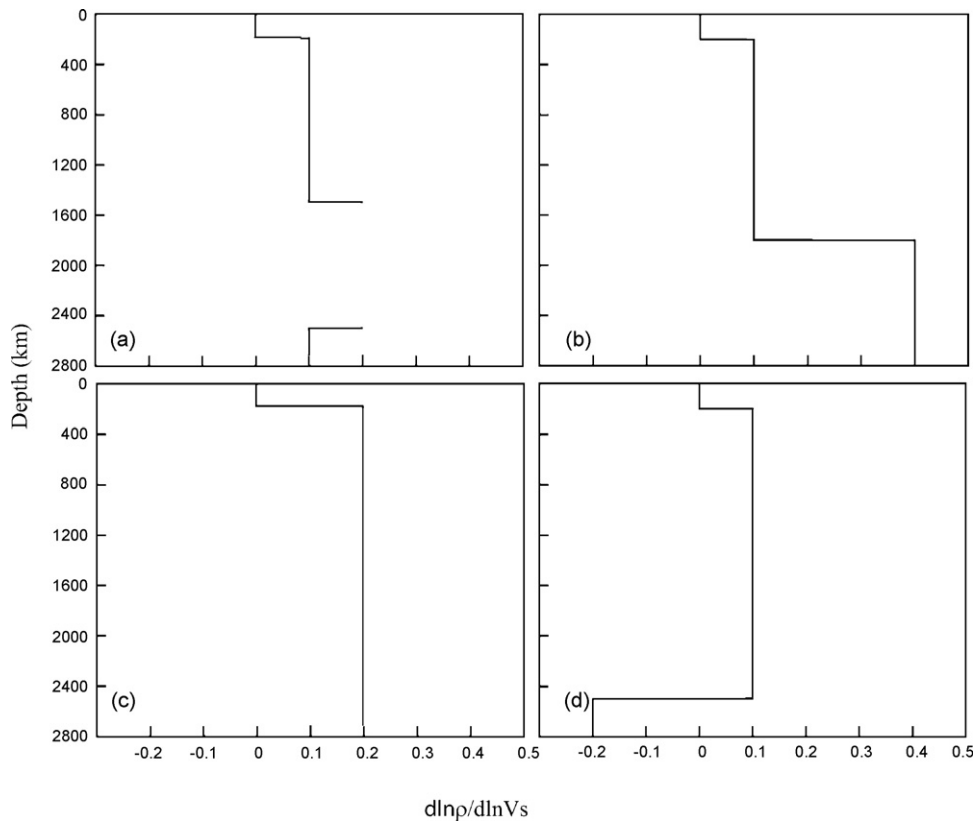


**Fig. 2.** The four shear-wave velocity–density scaling relationships used in this study inspired by previous studies (e.g., Gurnis et al., 2000; Karato and Karki, 2001; Steinberger and Calderwood, 2006; Steinberger and Holme, 2008).

This synthetic seismic model, derived by convolving the original numerical calculation with  $\mathbb{R}$ , features the blurring and smearing which compromise tomographic models and which may affect the accuracy of the global-scale flow field derived from the model. We use the same velocity–density scaling relationship as in the earlier step to convert the filtered wavespeed field back to temperature (i.e., to a buoyancy field) which we use as input to a calculation of the instantaneous global flow field using CitcomS to produce the global-scale velocity flow. This calculated flow field will be referred to as the “Tomography-Derived” flow field.

As the resolution operator is linear, it is possible to directly project the temperature field from the original convection calculation into the tomographic spatial parameterization and convolve it with  $\mathbb{R}$ . The filtered temperature field can then be converted to a wavespeed field using the relationships shown in Fig. 2.

### 3. Results

Fig. 3a shows the resulting temperature field (i.e., buoyancy field) derived from the 3D spherical geodynamical calculation (i.e., the GCM) projected onto a Cartesian box. Clusters of upwelling thermal plumes (red color) form beneath the Central Pacific and the African region while downwellings (blue color) are focused along the outer edge of the Pacific basin where lithosphere is subducting. We performed a resolution test using  $12 \times 96 \times 96 \times 96$  (from  $12 \times 64 \times 64 \times 64$ ) elements to verify that the small scale structures in the upper mantle (blue regions in the upper mantle in Fig. 3a) are not an artifact of the model resolution. We found that the temperature and flow fields for the model used here, and the higher resolution calculation were near-identical.

The global-scale mantle flow field associated with the GCM is shown at several depths in the mantle in Fig. 3c. Flow in the radial direction is shown as background color and flow in the lateral direc-

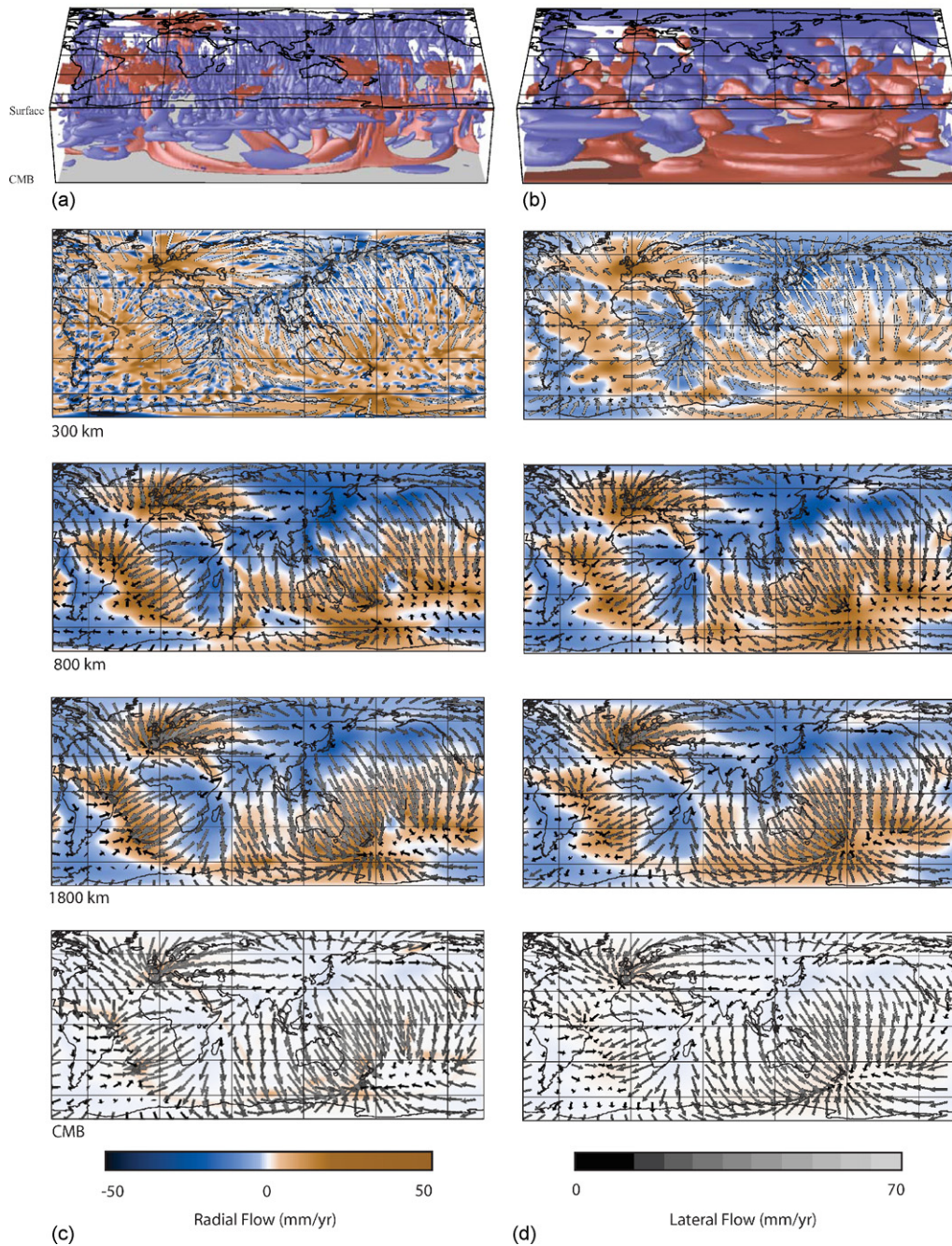
tion is shown as arrows, shaded according to magnitude. In the lowermost mantle the lateral flow is focused into areas of upwelling beneath the Central Pacific and along a N–W trend beneath the African region and away from areas of downwelling (i.e., along the edge of the Pacific basin). Higher in the lower mantle, the upwelling regions are broader but the lateral flow pattern is, to first order, the same as in the lowermost mantle, with flow into areas of upwelling and away from regions of subduction. In the upper mantle, the pattern of vertical flow is similar to flow in the lower mantle; however the direction of lateral flow is reversed, as material moves away from areas of upwelling (i.e., plume heads spread out) and moves towards areas of downwelling (i.e., subduction zones).

Fig. 3b shows the temperature field (i.e., buoyancy field) derived from the Tomography-Derived model projected onto a Cartesian box. Comparing this with the temperature field of the GCM (Fig. 3a) we note that the clusters of small upwelling plumes (red color) are now much broader, as  $\mathbb{R}$  has acted to blur and smooth the small-scale features from the GCM. The global mantle flow field from the Tomography-Derived model is shown at several depths in the mantle in Fig. 3d. For the case shown, we employ the density–velocity scaling relationship shown in Fig. 2a. The flow field has slightly lower magnitudes than the GCM flow field at all depths in the mantle, as seen by the lighter colors and flow arrows (compare Fig. 3d to Fig. 3c). One can apply a best fit factor to scale the Tomography-Derived flow field to account for the damping in the tomographic inversion (Ritsema et al., 2007 provides detailed discussion on how damping of the tomographic model influences the amplitudes of the synthetic anomalies). For the case shown, we find that a factor of 1.15 scales the amplitude of flow for the Tomography-Derived model to the amplitude of the GCM. In the lowermost mantle, the small upwellings observed in the GCM flow field (Fig. 3c, bottom panel) have been smeared into a more contiguous structure. This is also apparent in the upper mantle (compare top panels of Fig. 3c

and Fig. 3d) as the small scale radial flow patterns present in the GCM flow field have been blurred by the seismic filter and are not observed in the Tomography-Derived flow field. Throughout the rest of the mantle, the pattern of vertical flow is similar to the GCM flow field. The direction of flow changes very little between models as described below.

The angle between the 3D flow vectors of the two models is shown in Fig. 4a. To first order, throughout the mantle, the angle between the flow vectors of the two models is small ( $0\text{--}20^\circ$ ). Isolated regions beneath the Southern Atlantic and the Southern Pacific have much larger angles between the vectors, suggesting

that flow in this region predicted by the Tomography-Derived model differs strongly from that for the GCM model. These regions are present at all depths in the mantle, although the largest differences between flow vectors are seen in the lowermost mantle and above the transition zone. However, the majority of these misfits are located in regions where the velocity amplitudes are very small. We investigate the areas of poor angular correlation by comparing maps of the vertical resolution of the seismic model (Fig. 1) to the maps of angular correlation (Fig. 4a). In Fig. 1, areas of poor resolution are shown by brighter colors, and regions of good resolution appear as darker colors. The resolving power of the seismic



**Fig. 3.** The resulting 3D temperature field from (a) the whole-mantle convection calculation shown for the entire mantle and projected onto a Cartesian box and (b) the same convection calculation convolved with the resolution operator of S20RTS. In both cases clusters of upwelling thermal plumes form beneath the African region and the Southern Pacific (shown here in red), however the plumes in (b) are much broader due to the effect of the resolution operator. The resulting global-scale mantle flow fields from instantaneous Stokes flow calculations, which use (a) and (b) as their initial condition are shown in (c) and (d) respectively at 300 km, 800 km, 1800 km and 2800 km depth in the mantle.

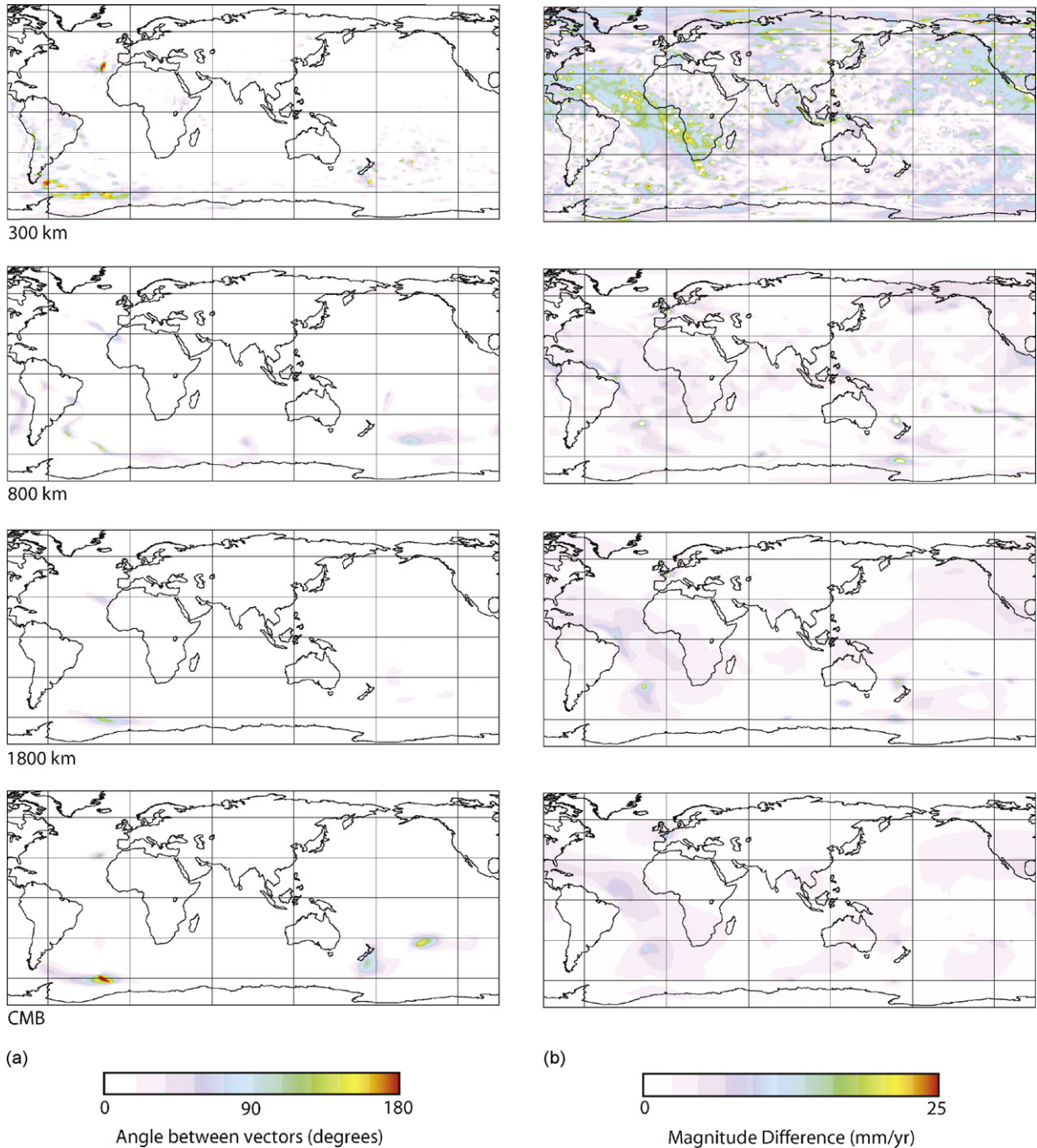


**Fig. 4.** (a) The angular difference between the 3D flow vectors of the GCM and the Tomography-Derived model shown at 300 km, 800 km, 1800 km and 2800 km depth in the mantle. Throughout most of the mantle, the angle between the vectors is relatively small. Several small regions, beneath the Southern Atlantic and the South Pacific show larger angles. (b) Magnitudinal differences between the 3D flow vectors of the GCM and the Tomography-Derived model shown at 300 km, 800 km, 1800 km and 2800 km depth in the mantle. The most significant magnitude differences occur in the upper mantle and in the lowermost mantle close to the CMB.

model has a maximum at 900 km depth and decreases with depth in the mantle. Throughout the mantle, the resolution of the seismic model is highest in the northern hemisphere, where coverage from sources and receivers is better than in the southern hemisphere. At all depths, regions of poor directional correlation in Fig. 4a are located, to first order, in areas of poor tomographic resolution in Fig. 1. This suggests that the Tomography-Derived flow field, which features significant damping, will vary most strongly from the GCM flow in regions where the resolution of the tomographic model is poor.

The average angular difference between the flow vectors as a function of depth is shown in Fig. 5a. Throughout the majority of

the mantle, the angle between the flow vectors is low (less than  $30^\circ$ ) and does not vary significantly with depth. A noticeable exception is found between  $\sim 500$  km and 700 km depth as the average angle between vectors increases to  $60^\circ$ . The decorrelation between vectors is sharp and at a maximum at  $\sim 520$  km depth.

Differences between the magnitudes of the velocity vectors of the GCM flow field and the Tomography-Derived flow field are given by:

$$\|\vec{v}\|_{control} - \|\vec{v}\|_{tomography} \quad (15)$$

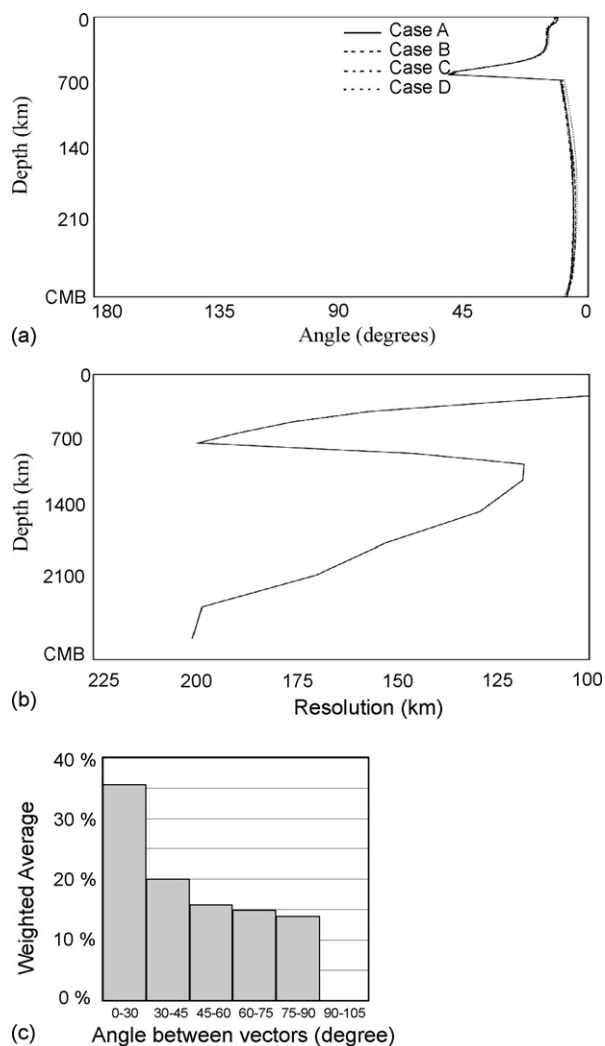


**Fig. 5.** (a) The average angular difference between the 3D flow vectors of the GCM and the Tomography-Derived model shown for the entire mantle. Note the peak at  $\sim 500$  km, which denotes a decorrelation between the flow vectors of the two models. (b) The average resolving power of S2ORTS shown for the entire mantle. Within the transition zone ( $\sim 500$  km to  $800$  km) there is a sharp decrease in the resolving power of the seismic model. This decrease agrees with the depths at which the decorrelation peak in (a) appears. (c) A histogram of the volume percentage of the mantle vs. angular distance between the flow vectors for the two models.

and are shown in Fig. 4b. Values close to 0 indicate regions where magnitudinal differences are minimal. The largest magnitude differences occur in the lowermost mantle close to the CMB and above the transition zone. At both depths, the resolution operator has the strongest effect on the vertical flow pattern (i.e., the small plumes in Fig. 3c, bottom and top panels, are smeared in Fig. 3d, bottom and top panels). Throughout the rest of the mantle, the magnitude differences are much smaller, albeit that the magnitudes of the GCM flow field are always higher than the Tomography-Derived flow field, as usually accepted due to the tomographic model being a damped representation of the true Earth structure: it is expected that a tomographic model will be more capable of resolving patterns of flow in the mantle, as opposed to the amplitude of flow.

The radial weighted-average of the resolving power of S2ORTS is shown in Fig. 5b (dashed line). Smaller values indicate regions where the resolution of the seismic model is highest. Within the transition zone (from  $\sim 800$  km to  $500$  km depth) there is a sharp decrease in the resolving power, as the structure is primarily constrained by surface-wave overtones, which have sensitivity over a broader depth range than the fundamental mode surface waves.

The diminishing resolution in the lower mantle is due to the wider separation of splines used to parameterize S2ORTS. Comparing Fig. 5a to Fig. 5b, there is a noticeable agreement of the depth at which the decorrelation of the vector directions occurs with the depth at which the resolving power of S2ORTS is at its poorest.

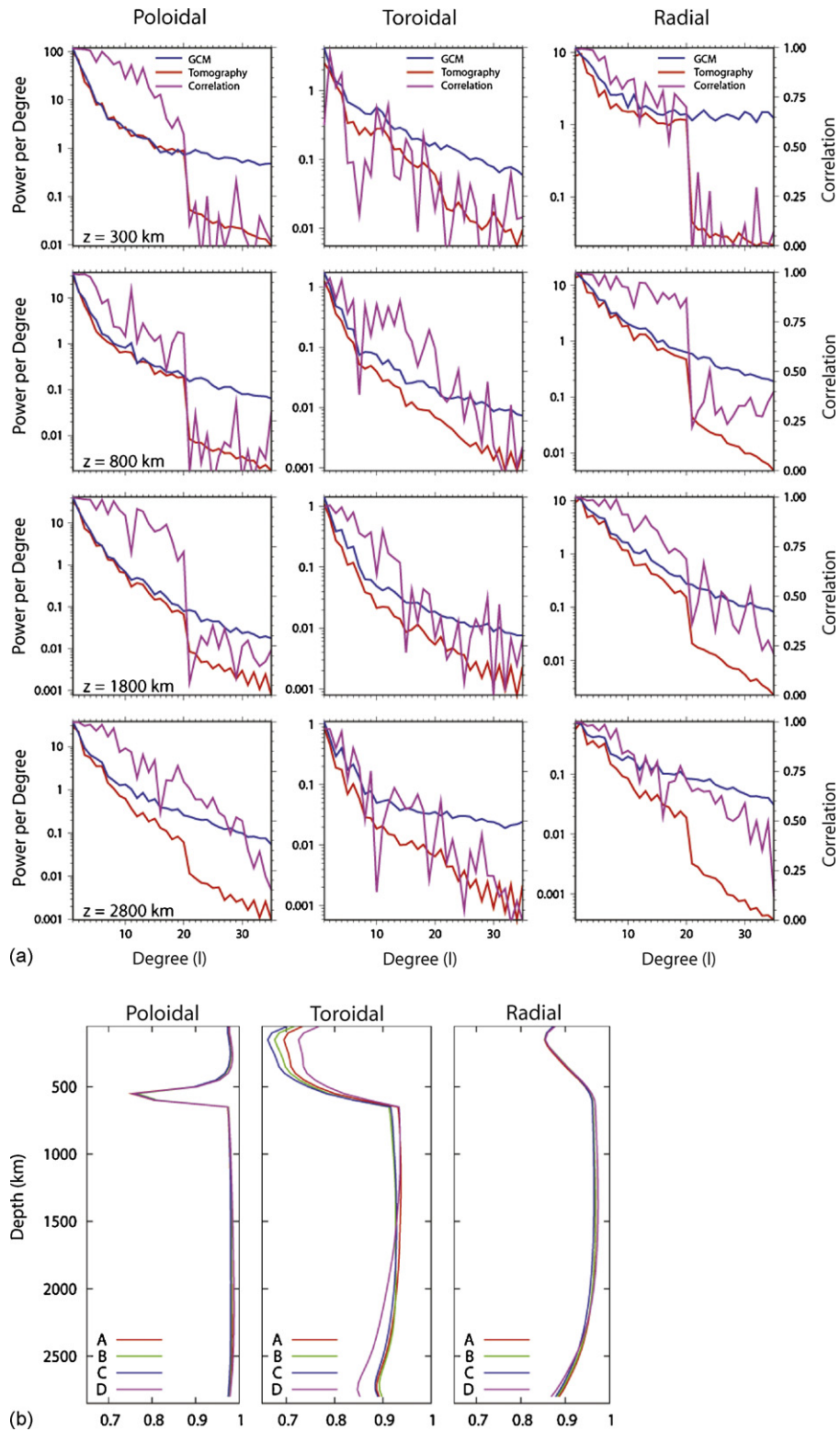
Fig. 6a shows RMS power and correlation for the Tomography-Derived and the GCM flow fields, at several depths in the mantle. For all components and at all depths in the mantle, the power of the Tomography-Derived model flow field decays more rapidly than the power of the GCM flow field. Such decay corresponds to a loss of short-wavelength flow due to damping in the tomographic inversion procedure. Above  $20^\circ$ , there is no power in the Tomography-Derived model, since S2ORTS is parameterized only up to  $20^\circ$ . Any structure above  $20^\circ$  is due to coupling to the lower degrees. Indeed, the aliasing to degrees higher than  $20^\circ$  for deep radial and poloidal flow is such that most degrees have positive correlation between models. We limit our comparisons of structure between the models to the long wavelength structure below  $20^\circ$ . Correlation between the GCM and the Tomography-Derived flow fields is greater than 0.75 for most depths for the poloidal and radial components. The toroidal component is less well matched.

Fig. 6b shows the correlation between the poloidal, toroidal and radial components of the GCM flow field and the flow fields for Cases A–D up to  $20^\circ$ . As noted in Fig. 5a, the correlation between models is low in the upper mantle and transition zone and high throughout the lower mantle. There is little difference in correlation and RMS power with depth for the four velocity–density scaling cases (Fig. 2) used in this study. The Tomography-Derived flow field for each case matches the GCM flow field quite well.

We performed the method outlined above for four different profiles of the velocity–density scaling value as shown in Fig. 2. The motivation is to investigate to what extent the resulting flow field depends on the density–velocity ratio chosen. The four profiles differ in their radial structure of  $R$ . We find, however, that for all four profiles, the results are very similar. The directions of the flow field for each profile correlate strongly at all depths with the flow directions from the GCM (i.e., the plots shown in Fig. 4a are near-identical for all of the relationships shown in Fig. 2). As before, areas of poor correlation are located in regions where the resolution of the seismic model is at its lowest. The magnitudes of the Tomography-Derived flow fields vary slightly with each density–velocity profile; however the pattern of flow (i.e., shape of upwellings and downwellings) does not change and the differences in magnitudes were very small.

#### 4. Discussion

In this work, we investigated possible caveats associated with using seismic observations to calculate flow fields. As global-scale mantle flow fields are widely used in many aspects of geophysics, such as seismic anisotropy studies (e.g., Becker et al., 2003; Behn et al., 2004), investigations of tectonic driving forces (e.g., Lithgow-Bertelloni and Silver, 1998; Becker and O’Connell, 2001; Conrad and Lithgow-Bertelloni, 2002) it is important to have constraints on the reliability of the method used to derive the flow field. Although previous authors (e.g., Becker and O’Connell, 2001; Bunge et al., 2002; Becker, 2006; Simmons et al., 2006; Steinberger and Calderwood, 2006; Forte, 2007; Steinberger and Holme, 2008) have investigated various aspects of geodynamically and seismically derived global mantle flow fields (viscosity structure, density–velocity conversion factor, etc.) this paper presents the first attempt to investigate the method of using seismic observations to constrain mantle flow and to numerically compare geodynamically derived and seismically derived global-scale mantle flow field models. This study, which is complimentary to the work of Becker and Boschi (2002) and Becker



**Fig. 6.** (a) RMS power and correlation for the Tomography-Derived flow field and the GCM flow field shown at 300 km, 800 km, 1800 km and 2800 km depth in the mantle. The left, center and right columns show the poloidal, toroidal and radial components respectively. Spherical harmonic power per degree and unit area is shown as a blue line (GCM flow field) and a red line (Tomography-Derived flow field) plotted against a log scale on the left. The correlation between the two models per degree is shown by the magenta curve and is plotted against a linear scale on the right. (b) Correlation between the poloidal, toroidal and radial components of the GCM flow field and the Tomography-predicted flow fields for Cases A–D up to  $20^\circ$ .

(2006), reveals that the method of deriving global-scale mantle flow fields from seismic tomography observations is reliable, and as such, will provide a valuable resource for those using such global flow fields to study other aspects of the Earth.

Fig. 5c shows a histogram of the volume percentage of the mantle vs. angular distance between the flow vectors for the two models. The histogram shows that for 36% of the mantle, the angular differences are less than  $30^\circ$  and for over 56% of the mantle, angu-

lar differences are less than  $45^\circ$ , suggesting that flow directions predicted by the Tomography-Derived model do not differ greatly from GCM flow directions. For many studies, this may provide more-than-adequate resolution of flow direction; however, this also suggests that one must be cautious when using tomography-derived flow fields in work that may require better directional control than  $\sim 30^\circ$ , such as comparing predicted vs. observed shear wave splitting directions. The Tomography-Derived flow field correlated well with the GCM flow field at most depths in the mantle. The best correlation was in the mid- and lower mantle, between 800 km and 2000 km. At these depths, the resolving power of the seismic model is high and the “seismic filter” has little effect on the original buoyancy field. The poorest correlation was in the transition zone, in agreement with the depth at which the resolution of S20RTS is at its poorest. Furthermore, this region of the model is dynamically complex because of the viscosity increase from the low viscosity upper mantle to a higher viscosity lower mantle.

We note that the near-surface flow velocities predicted by the Tomography-Derived model do not resemble plate motions. In this study, we are interested in the global-scale bulk mantle flow, rather than comparing asthenospheric flow vectors with true plate motions, and as such make no special treatment of lithospheric plates, plate motions or continental keels. The formulation employed in this work leads to a rigid lid due to the values of the average temperature used in the conversion from density to velocity fields and to the free-slip boundary conditions employed in the one-step Stokes flow calculation. Thus, we do not expect flow in the shallow mantle to resemble observed flow (i.e., plate motions). Instead, we focus on how the heterogeneous nature of tomographic resolution affects large-scale mantle flow.

We used only one tomography model in this work. Different seismic models are created from different data sets, and as such, it would be of value to the community to perform a similar study, looking at several seismic models, to thoroughly investigate the effect of the resolution operator on global flow fields. We did not include the effect of composition in our geodynamic model. Most global mantle flow studies assume homogeneous composition when determining tomography-derived buoyancy fields and accordingly, we applied the same assumption to our study in order to better evaluate this method. Recent work has suggested, however, that numerical models which involve a thermochemical component (e.g. Tackley, 1998, 2002; Davaille, 1999; Kellogg et al., 1999; Ni et al., 2002; Jellinek and Manga, 2004; McNamara and Zhong, 2004, 2005; Tan and Gurnis, 2005, 2007; Simmons et al., 2007; Bull et al., 2009) result in a lower-mantle structure which better resembles the observed mantle structure than models with purely isochemical convection (e.g., Bunge et al., 1998; Richards et al., 2000; McNamara and Zhong, 2005). If a thermochemical component does exist, its composition is unknown, and as such, employing a compositional-dependence of seismic wavespeed into our models would introduce several new unknown parameters (composition of material, volume of material, amount of entrainment of mantle material). Also, compositional anomalies in the mantle would possibly be ubiquitous and laterally varying. Finally, one should recognize the uncertainties associated with the numerical modeling. We chose our parameters as best estimates of Earth-consistent material properties, however many parameters remain poorly constrained (i.e., viscosity, internal heating, thermal expansivity). It is important however to note that in this work, we are focused on evaluating one method used to calculate global-scale mantle flow fields, and not to model the actual Earth.

## 5. Conclusions

In this work, we investigated several possible caveats associated with using seismic observations to calculate flow fields: (1)

the resolving power of the tomographic model may affect the calculated flow field and (2) the relationship used to interpret seismic anomalies in terms of density is not well-constrained over the depth of the mantle.

We find these general conclusions.

- (1) The global-scale mantle velocity flow field predicted by the Tomography-Derived model correlates well with the flow field predicted by the GCM throughout most of the mantle. In regions where the resolving power of S20RTS is at its lowest, the agreement between flow fields decreases, however, such regions account for less than 30% of the entire mantle.
- (2) The Tomography-Derived flow field is relatively independent of the density–velocity scaling ratio used: the direction of flow is relatively unchanged between scaling ratios, and the magnitude of flow is only slightly affected.

## Acknowledgements

The authors would like to thank Dr. S.D. King and Dr. C. Beghein for their constructive reviews and insightful comments. Discussions with Dr. A. Clarke, Dr. M. Fouch, Dr. E. Garnero and Dr. J. Tyburczy aided greatly in the creation of the final manuscript. The authors would also like to extend gratitude to Dr. F. Timmes for access to ASU's high performance computing center which was invaluable to this research. The work in this manuscript was supported by grants NSF: EAR-0838565 and NSF: EAR-0510383.

## References

- Becker, T.W., O'Connell, R.J., 2001. Predicting plate velocities with geodynamic models. *Geochem. Geophys. Geosyst.* 2, doi:10.1029/2001GC000171.
- Becker, T.W., Boschi, L., 2002. A comparison of tomographic and geodynamic mantle models. *Geochem. Geophys. Geosyst.* 3 (1), 1003, doi:10.1029/2001GC000168.
- Becker, T.W., Kellogg, J.B., Ekström, G., O'Connell, R.J., 2003. Comparison of azimuthal seismic anisotropy from surface waves and finite-strain from global mantle-circulation models. *Geophys. J. Int.* 155, 696–714.
- Becker, T.W., 2006. On the effect of temperature and strain-rate dependent viscosity on global mantle flow, net rotation, and plate-driving forces. *Geophys. J. Int.* 167, 943–957.
- Behn, M.D., Conrad, C.P., Silver, P.G., 2004. Detection of upper mantle flow associated with the African superplume. *Earth Planet. Sci. Lett.* 224, 259–274.
- Bull, A.L., McNamara, A.K., Ritsema, J., 2009. Synthetic tomography of plume cluster and thermochemical piles. *Earth Planet. Sci. Lett.* 278, 152–162.
- Bunge, H.-P., Richards, M.A., Lithgow-Bertelloni, C., Baumgardner, J.R., Grand, S.P., Romanowicz, B.A., 1998. Time-scales and heterogeneous structure in geodynamic Earth models. *Science* 280, 91–95.
- Bunge, H.-P., Richards, M.A., Baumgardner, 2002. Mantle-circulation models with sequential data assimilation: inferring present-day mantle structure from plate motion histories. *Philos. Trans. Roy. Soc. Lond. A* 360, 2545–2567.
- Cadek, O., Fleitout, L., 1999. A global geoid model with imposed plate velocities and partial layering. *J. Geophys. Res.* 104, 29055–29075.
- Cammarano, F., Goes, S., Vacher, P., Giardini, D., 2003. Inferring upper-mantle temperatures from seismic velocities. *Phys. Earth Planet. Int.* 138, 197–222.
- Chopelas, A., 1992. Sound velocities of MgO to very high compression. *Earth Planet. Sci. Lett.* 114, 185–192.
- Conrad, C.P., Lithgow-Bertelloni, C., 2002. How mantle slabs drive plate tectonics. *Science* 298, 207–209.
- Conrad, C., Behn, M.D., Silver, P.G., 2007. Global mantle flow and the development of seismic anisotropy: differences between the oceanic and continental upper mantle. *J. Geophys. Res.* 112, B07317, doi:10.1029/2006JB004608.
- Davaille, A., 1999. Simultaneous generation of hotspots and superwells by convection in a heterogeneous planetary mantle. *Nature* 402, 756–760.
- Davies, J.H., Bunge, H.-P., 2001. Seismically “fast” geodynamic mantle models. *Geophys. Res. Lett.* 28 (1), 73–76.
- Dziewonski, A.M., Hager, B.H., O'Connell, R.J., 1977. Large-scale heterogeneity in the lower mantle. *J. Geophys. Res.* 82, 239–255.
- Dziewonski, A.M., 1984. Mapping the lower mantle: determination of lateral heterogeneity in P velocity up to degree and order 6. *J. Geophys. Res.* 89, 5929–5952.
- Forte, A.M., Peltier, W.R., 1987. Plate tectonics and a spherical earth structure: the importance of poloidal–toroidal coupling. *J. Geophys. Res.* 92, 3645–3679.
- Forte, A.M., Peltier, W.R., 1991. Viscous flow models of global geophysical observables. 1. Forward problems. *J. Geophys. Res.* 96, 20131–20159.
- Forte, A.M., Mitrovica, J.X., 2001. Deep-mantle high viscosity flow and thermochemical structure inferred from seismic and geodynamic data. *Nature* 410, 1049–1056.

- Forté, A.M., Woodward, R.L., Dziewonski, A.M., 1994. Joint inversions of seismic and geodynamic data for models of three-dimensional mantle heterogeneity. *J. Geophys. Res.* 99, 21857–21877.
- Forté, A.M., Dziewonski, A.M., O'Connell, R.J., 1995. Continent-ocean chemical heterogeneity in the mantle based on seismic tomography. *Science* 268, 386–388.
- Forté, A.M., 2007. Constraints on seismic models from other disciplines: implications for mantle dynamics and composition. In: Schubert, G., Bercovici, D. (Eds.), *Treatise on Geophysics*, pp. 805–858.
- Gaboret, C., Forté, A.M., Montagner, J.-P., 2003. The unique dynamics of the Pacific Hemisphere mantle and its signature on seismic anisotropy. *Earth Planet. Sci. Lett.* 208, 219–233.
- Gurnis, M., Mitrovica, J.X., Ritsema, J., van Heijst, H.-J., 2000. Constraining mantle density structure using geological evidence of surface uplift rates: the case of the African superplume. *Geochim. Geophys. Res.* 10, 1999GC000035.
- Hager, B.H., O'Connell, R.J., 1981. A simple global model of plate dynamics and mantle convection. *J. Geophys. Res.* 86, 4843–4867.
- Hager, B.H., Clayton, R.W., Richards, M.A., Comer, R.P., Dziewonski, A.M., 1985. Lower mantle heterogeneity, dynamic topography and the geoid. *Nature* 313, 541–545.
- Hager, B.H., Clayton, R.W., 1989. Constraints on the structure of mantle convection using seismic observations, flow models and the geoid. In: Peltier, W.R. (Ed.), *Mantle Convection: Plate Tectonics and Global Dynamics*. Gordon and Breach, New York, pp. 657–763.
- Hager, B.H., Richards, M.A., 1989. Long-wavelength variations in Earth's geoid: physical models and dynamical implications. *Philos. Trans. Roy. Soc. Lond. A* 328, 309–327.
- Jellinek, A.M., Manga, M., 2004. Links between long-lived hotspots, mantle plumes, D" and plate tectonics. *Rev. Geophys.* 42, RG3002, doi:10.1029/2003RG000144.
- Jordan, T.H., 1978. Composition and development of the continental tectosphere. *Nature* 274, 544–548.
- Karato, S., 1993. Importance of elasticity in the interpretation of seismic tomography. *Geophys. Res. Lett.* 20, 1623–1626.
- Karato, S.-I., Karki, B.B., 2001. Origin of lateral variation of seismic wave and velocities and density in the deep mantle. *J. Geophys. Res.* 106, 21771–21783.
- Kellogg, L.H., Hager, B.H., van der Hilst, R.D., 1999. Compositional stratification in the deep mantle. *Science* 283, 1881–1884.
- King, S.D., Masters, G., 1992. An inversion for radial viscosity structure using seismic tomography. *Geophys. Res. Lett.* 19, 1551–1554.
- King, S.D., 1995. Radial models of mantle viscosity. Results from a genetic algorithm. *Geophys. J. Int.* 122, 725–734.
- Lithgow-Bertelloni, C., Richards, M.A., 1998. The dynamics of Cenozoic and Mesozoic plate motions. *Rev. Geophys.* 36, 27–78.
- Lithgow-Bertelloni, C., Silver, P.G., 1998. Dynamic topography, plate driving forces and the African superswell. *Nature* 395, 269–272.
- Lithgow-Bertelloni, C., Gynn, J.H., 2004. Origin of the lithospheric stress field. *J. Geophys. Res.* 109, B01408, doi:10.1029/2003JB002467.
- Matas, J., Bukowski, M.S.T., 2007. On the anelastic contribution to the temperature dependence of lower mantle seismic velocities. *Earth Planet. Sci. Lett.* 259, 51–65.
- McNamara, A.K., Zhong, S., 2004. Thermochemical structures within a spherical mantle: superplumes or piles? *J. Geophys. Res.* 109, B07402, doi:10.1029/2003JB002847.
- McNamara, A.K., Zhong, S., 2005. Thermochemical structures beneath Africa and the Pacific. *Nature* 437, 1136–1139.
- Mégnin, C., Bunge, H.-P., Romanowicz, B., Richards, M.A., 1997. Imaging 3D spherical convection models: what can seismic tomography tell us about mantle dynamics? *Geophys. Res. Lett.* 24, 1299–1302.
- Ni, S., Tan, E., Gurnis, M., Helmberger, D.V., 2002. Sharp sides to the African superplume. *Science* 296, 1850–1852.
- Resovsky, J., Trampert, J., 2003. Using probabilistic seismic tomography to test mantle velocity–density relationships. *Earth Planet. Sci. Lett.* 215, 121–134.
- Ricard, Y., Fleitout, L., Froidevaux, C., 1984. Geoid heights and lithospheric stresses for a dynamic Earth. *Ann. Geophys.* 2, 267–286.
- Ricard, Y., Vigny, C., 1989. Mantle dynamics with induced plate tectonics. *J. Geophys. Res.* 94, 17543–17559.
- Ricard, Y., Vigny, C., Froidevaux, C., 1989. Mantle heterogeneities, geoid and plate motion: a Monte-Carlo inversion. *J. Geophys. Res.* 94, 13739–13754.
- Richards, M.A., Hager, B.H., 1984. Geoid anomalies in a dynamic Earth. *J. Geophys. Res.* 89, 5987–6002.
- Richards, M.A., Bungler, H.-P., Lithgow-Bertelloni, C., 2000. Mantle convection and plate motion history: toward general circulation models. In: Richards, M.A., et al. (Eds.), *The History and Dynamics of Global Plate Motions*. Geophysical Monograph Series, vol. 121. American Geophysical Union, pp. 289–307.
- Ritsema, J., van Heijst, H.J., Woodhouse, J.H., 1999. Complex shear-wave velocity structure imaged beneath Africa and Iceland. *Science* 286, 1925–1928.
- Ritsema, J., van Heijst, H.J., Woodhouse, J.H., 2004. Global transition zone tomography. *J. Geophys. Res.* 109, B02302, doi:10.1029/2003JB002610.
- Ritsema, J., McNamara, A.K., Bull, A.L., 2007. Tomographic filtering of geodynamic models: implications for model interpretation and large-scale mantle structure. *J. Geophys. Res.* 112, B01303, doi:10.1029/2006JB004566.
- Schubert, G., Masters, G., Olsen, P., Tackley, P.J., 2004. Superplumes or plume clusters? *Phys. Earth Planet. Int.* 146, 147–162.
- Schuberth, B.S.A., Bunge, H.-P., Ritsema, J., 2009. Tomographic filtering of high-resolution mantle circulation models: can seismic heterogeneity be explained by temperature alone? *Geochem. Geophys. Res.* 10, Q05W03, 18pp. doi:10.1029/2009GC002401.
- Simmons, N.A., Forté, A.M., Grand, S.P., 2006. Constraining mantle flow with seismic and geodynamic data: a joint approach. *Earth Planet. Sci. Lett.* 246, 109–124.
- Simmons, N.A., Forté, A.M., Grand, S.P., 2007. Thermochemical structures and dynamics of the African superplume. *Geophys. Res. Lett.* 34, L02301, doi:10.1029/2006GL028009.
- Soldati, G., Boschi, L., 2005. The resolution of whole Earth seismic tomographic models. *Geophys. J. Int.* 161, 143–153.
- Steinberger, B., Schmeling, H., Marquart, G., 2001. Large-scale lithospheric stress field induced by global mantle circulation. *Earth Planet. Sci. Lett.* 186, 75–91.
- Steinberger, B., Calderwood, A.R., 2006. Models of large-scale viscous flow in the Earth's mantle with constraints from mineral physics and surface observables. *Geophys. J. Int.* 167, 1461–1481.
- Steinberger, B., Holme, R., 2008. Mantle flow models with core–mantle boundary constraints and chemical heterogeneities in the lowermost mantle. *J. Geophys. Res.* 113, B05403.
- Stixrude, L., Lithgow-Bertelloni, C., 2005. Thermodynamics of mantle minerals—1. Physical properties. *Geophys. J. Int.* 162, 610–632.
- Tackley, P.J., 1998. Three-dimensional simulations of mantle convection with a thermochemical CMB boundary layer: D"? In: Gurnis, et al. (Eds.), *The Core–Mantle Boundary Region*. American Geophysical Union, pp. 231–253.
- Tackley, P.J., 2002. Strong heterogeneity caused by deep mantle layering. *Geochem. Geophys. Res.* 3, doi:10.1029/2001GC000167.
- Tan, E., Gurnis, M., 2005. Metastable superplumes and mantle compressibility. *Geophys. Res. Lett.* 32, L20307, doi:10.1029/2005GL024190.
- Tan, E., Gurnis, M., 2007. Compressible thermochemical convection and application to lower mantle structures. *J. Geophys. Res.* 112, B06304, doi:10.1029/2006JB004505.
- Thoraval, C., Richards, M.A., 1997. The geoid constraint in global geodynamics: viscosity structure, mantle heterogeneity models and boundary conditions. *Geophys. J. Int.* 131, 1–8.
- Woodhouse, J.H., Dziewonski, A.M., 1984. Mapping the upper mantle: three dimensional modeling of the Earth structure by inversion of seismic waveforms. *J. Geophys. Res.* 89, 5953–5986.
- Zhong, S., Zuber, M.T., Moresi, L., 2000. Role of temperature-dependent viscosity and surface plates in spherical shell models of mantle convection. *J. Geophys. Res.* 105, 11063–11082.